RSC Advances

ROYAL SOCIETY OF CHEMISTRY

www.rsc.org/advances

A novel nanocomposite for bone tissue engineering based on chitosan-silk sericin/hydroxyapatite: biomimetic synthesis and its cytocompatibility

Li Chen [a,b], Jingxiao Hu [a], Jiabing Ran [a], Xinyu Shen [a]*, Hua Tong [a]*

[a] Key Laboratory of Analytical Chemistry for Biology and Medicine, Ministry of Education, College of Chemistry and Molecular Sciences, Wuhan University, Wuhan 430072, China

[b] Department of Urban Construction, City College, Wuhan University of Science and Technology, Wuhan 430083, China

* Corresponding author. Tel.: +86 27 68764510; fax: +86 27 68752136

E-mail address: tonghua@whu.edu.cn (H. Tong); shenxy@whu.edu.cn (XY. Shen)

Abstract: A simple and effective approach was developed to synthesize chitosan-silk sericin /hydroxyapatite nanocomposites by in situ precipitation and two ways of alkali diffusion were carried out in this study. The objective of this paper was to investigate the different properties of the nanocomposites. SEM showed that the rod-like hydroxyapatite particles with a diameter of 20-50 nm were distributed homogeneously within the chitosan-silk sericin matrix, and the formation mechanism was also investigated. The results of FTIR and XRD indicated that the inorganic phase in the nanocomposite was carbonate-substituted hydroxyapatite with low crystallinity. In terms of mechanical properties, chitosan-silk sericin/hydroxyapatite nanocomposites exhibited a higher elastic modulus and compressive strength than that of the chitosan/hydroxyapatite nanocomposites. *In vitro* cytocompatibility of the nanocomposite was evaluated by CCK-8 assay and SEM through MG63 osteoblast cells cultured on the samples, which demonstrated that they are non-toxic and support cell growth. These results suggest that the chitosan-silk sericin/hydroxyapatite nanocomposites are promising biomaterials for bone tissue engineering.

Keywords: chitosan; silk sericin; hydroxyapatite; bone tissue engineering

1 Introduction

Autograft and allograft are considered ultimate for bone grafting procedure providing osteoconductive and osteoinductive growth factors. However, limitations in donor site, additional surgery, disease transmission and expenditure poses a need to develop alternatives to autograft and allograft [1,2]. Bone tissue engineering is an emerging technique that offers potential solutions to these problems. Bone tissue engineering is a rapidly developing discipline used in order to repair, replace and regenerate injured bone tissue [3]. In bone tissue the extracellular matrix (ECM) consists of an organic phase made of type I and type III collagen and glycosaminoglycans (GAGs) and an inorganic phase made up of hydroxyapatite [4].

Chitosan (CS) is a linear polysaccharide derived by partial N-deacetylationof chitin, which is the primary structural polymer in arthropod exoskeletons, shells of crustaceans, or the cuticles of insects [5]. CS is widely applied in bone tissue engineering because of its special characteristics, such as structural similarity to the various glycosaminoglycans found in the ECM of bone, osteoconductivity to enhance bone formation both *in vitro* and *in vivo*, good biodegradability, and excellent biocompatibility [6-8]. Moreover, the cationic nature of CS allows for mimicking the ECM-rich environment of bone tissue through the formation of insoluble ionic complexes with anionic molecules, for instance, glycosaminoglycans, proteoglycans and growth factors, which promote cell growth, proliferation, differentiation and tissue formation [9, 10]. However, its bioactivity isn't good enough for bone tissue engineering and it is frequently combined with biologically active materials like collagen, silk sericin and hydroxyapatite [11]. Hydroxyapatite (HA, $Ca_{10}(PO_4)_6(OH)_2$), is one of the known biocompatible ceramic which has significant chemical, compositional, biological, and crystal structure resemblance to the mineral constituents of human skeleton [12]. It is well known that HA has been currently used in bone tissue engineering due to its excellent bioactivity and biocompatibility [13]. Furthermore, the osteoconduction, non-inflammation and non-toxicity of HA enable osteoblast adhesion, proliferation and differentiation. HA has a unique ability of binding to the natural bone through biochemical bonding, which promotes the interaction between host bone and grafted material [14, 15]. Currently, there are some techniques

concerning preparing CS/HA composite materials, including co-precipitation [16], alternate soaking [17] and mechanical mixing [18]. Among these methods, there is a common shortcoming that inorganic particles cannot be distributed homogeneously in the organic matrices at nanolevel, which leads to poor mechanical properties and limits their applications.

Though collagen had the similar organic constitution to the natural bone, the collagen derived from animal tissues may cause many concerns related to the purity, quality and some diseases. In addition, the mechanical strength of the collagen is not high enough and its degradation rate is too fast. Therefore, selecting a noncollagen protein as the organic matrix is also an ideal way. In comparison with collagen, Silk sericin (SS) can be more easily extracted, and is more accessible because of wide range of sources as well as its low cost. SS is a protein secreted from the middle silk gland of a mature silkworm larva and acts as the glue for adhesion of fibroin based fibers during cocoon formation [19,20]. The glue-like protein is composed of random coil and β-sheet secondary structures with a high abundance of hydrophilic amino acids that confers water solubility [21-23]. Moreover, recent studies have found unique characteristics of SS, such as heterogeneous nucleation of apatite [24], and induce collagen production [25,26] without the activation of pro-inflammatory cytokines [27]. Especially, it has been proved that silk sericin supports cell adhesion and proliferation when used in pure form and blended in matrices [28]. Minoura et al [29] reported that silk sericin enhances the attachment and growth of mouse fibroblast when used as a substratum as high as collagen. In a dose dependent manner, SS accelerates proliferation of mammalian cells line in culture [30]. In addition, SS has been also shown to enhance functionality in promoting osteoblast adhesion, proliferation, and alkaline phosphatase activity [31]. Hence, SS was introduced into the CS/HA system to enhance the cytocompatibility of CS/HA nanocomposite.

However, SS has received less attention in tissue engineering applications because of its weak structural properties (difficult to form shapes) and high water solubility. Formerly, many attempts were used to solve the problem on fabrication of the SS, for example, cross-linking [32-34], blending [35], or copolymerization it with other substances [36]. Silk sericin consists of polar side chain made of hydroxyl, carboxyl and amino groups that enable sensitivity to

chemical modification [37]. In order to improve SS's weak structural properties, combining chitosan and silk sericin with hydroxyapatite and cross-linking method were adopted in this research.

The purpose of this study was to fabricate homogeneous CS-SS/HA nanocomposites by the in situ precipitation approach, which is totally different from the traditional ones and rarely reported in the synthesis of CS-SS/HA composites. Compared with other methods, the superiority of in situ precipitation is unique morphology and ultrafine HA particles can be produced, and moreover, distributed homogeneously within the organic template. What's more, it is worth noting that this method had another important merit that the products had no other impure inorganic component except HA in composition by comparison with other in situ precipitation methods. In the present study chitosan-silk sericin hydrogel cross-linked by genipin was constructed. To our knowledge, chemical crosslinkers were now applied in the crosslinking of CS, including glutaraldehyde [38], epichlorohydrin [39], EDC [40], ethylene glycol diglycidyl ether [41] and so forth. Nevertheless, these crosslinking agents are toxic and may impair the biocompatibility of biomaterials. Genipin exhibits low cytotoxicity as compared to other crosslinking reagents, and has also been reported as a crosslinker for CS [42-45]. Unlike the previous work [46-48], two ways of alkali diffusion were carried out in this study. The morphology and composition of as-synthesized nanocomposites were mainly analyzed by Fourier transform infrared spectroscopy (FT-IR), X-ray diffraction (XRD), field emission scanning electron microscopy (SEM), and transmission electron microscopy (TEM). The mechanical performance of these samples was also investigated. The cytotoxicity of silk sericin was finally evaluated based on MG63 osteoblast cells morphologic changes and the CKK-8 assay evaluation.

2 Materials and Methods

2.1 Materials

Chitosan (Mw 1,000,000) was obtained from Golden-Shell Biochemical Co. (Zhejiang, China) with 95% degree of the deacetylation. Bombyx mori silk sericin (Mw=30,000) was purchased from Huzhou Xintiansi Biotechnology Co.,

Ltd. (China). Genpin was purchased from Chengdu ConBon Bio-tech CO., Ltd. (China). Calcium nitrate tetrahydrate ($Ca(NO_3)_2 \cdot 4H_2O$), diammonium hydrogen phosphate ($(NH_4)_2HPO_4$), acetic acid and ammonia were purchased from Sinopharm Chemical Reagent Co., Ltd. (Shanghai, China). All the reagents used in this work were of analytical grade (AR) and used without any further purification. Deionized ultrapure water was used throughout the experiment.

2.2 Methods

2.2.1 Synthesis of CS-SS/HA-s nanocomposites by in situ precipitation

CS solution was prepared by dissolving CS in 40 ml of acetic acid solution (2 vol.%) with continuously stirring at 45 ºC until it became perfectly transparent. Then SS powder was added into the CS solution and stirred at 45 ºC for 30 min. Afterwards, $Ca(NO_3)_2 \cdot 4H_2O$ and $(NH_4)_2HPO_4$ (Ca/P=1.67) were together added to the mixed solution under agitation until the salts were entirely dissolved. Subsequently, 0.048 g genpin was added to the previous mixed solution as a crosslinking agent. The solution was continuously stirred until a blue hydrogel formed. The resulting hydrogel was then stored under ambient conditions for 24 h to reach complete crosslinking. Ammonia solution was then poured on the top of the blue hydrogel at room temperature. Under this alkaline condition, HA precipitated within the hydrogel gradually. The in situ precipitation method can be represented by the following chemical reaction:

$$10Ca^{2+} + 6HPO_4^{2-} + 8OH^- + Ca_{10}(PO_4)_6(OH)_2(\downarrow) + 6H_2O \quad (pH > 10)$$

The nanocomposite was finally washed with disilled water until the pH of eluate was about 7, followed by drying at room temperature to obtain the solid nanocomposite. The starting content of all reagents was scaled according to the final organic/HA weight ratio of 70/30, 60/40, 50/50, 40/60 and 30/70. and the initial amounts of the reagents used in this work are listed in Table 1. The weights of HA, $Ca(NO_3)_2 \cdot 4H_2O$ and $(NH_4)_2HPO_4$ were calculated according to above equation. The synthetic routes for the preparation of CS-SS/HA-s nanocomposites were shown in Fig. 1.

2.2.2 Synthesis of CS/HA-s nanocomposites by in situ precipitation

CS/HA nanocomposites with different organic/inorganic weight ratios as control samples were also prepared through in situ precipitation. The above-mentioned process has been repeated in the absence of SS to fabricate the CS/HA-s

nanocomposites. The starting content of all reagents was scaled according to the final organic/HA weight ratio of 70/30, 60/40, 50/50, 40/60 and 30/70. and the initial amounts of the reagents used in this work are listed in Table 1. The weights of HA, $Ca(NO_3)_2 \cdot 4H_2O$ and $(NH_4)_2HPO_4$ were calculated according to above equation.

2.2.3 Synthesis of CS-SS/HA-g nanocomposites by in situ precipitation

The preparing procedures are the same as described in Section 2.2.1, but the way of alkali diffusion was changed. The blue hydrogel and ammonia solution were together put into a closed environment through ammonia volatilization. The nanocomposite was finally washed with disilled water until the pH of eluate was about 7, followed by drying at room temperature to obtain the solid nanocomposite. The starting content of all reagents was scaled according to the final organic/HA weight ratio of 70/30, 60/40, 50/50, 40/60 and 30/70. and the initial amounts of the reagents used in this work are listed in Table 1. The weights of HA, $Ca(NO_3)_2 \cdot 4H_2O$ and $(NH_4)_2HPO_4$ were calculated according to above equation. The process for the fabrication of CS-SS/HA-g nanocomposites was displayed in Fig. 1.

2.2.4 Characterization

Morphology of inorganic/organic composite was observed using Environmental Scanning Electron Microscopy (SEM, Quanta200, FEI, Holland and SEM, Sigma, Zeiss, Germany) and field emission transmission electron microscope (2010FEF, JOEL, Japan). The crystalline phase and component of obtained products were identified using wide angle X-ray diffraction analysis (XRD, X'pert PRO, Panalytical, Holland) and Fourier Transform Infrared Spectrometer (FT-IR, Nicolet5700, America). Amino acid composition analysis was performed by a HITACHI-835 Amino Acid Analyzer. Samples were hydrolyzed with 6 M HCl at 110 ºC for 24 h. The hydrolyzate was diluted with water to 25 mg/ml and the diluted solution was analyzed.

Mechanical properties tests were measured at room temperature by a universal testing machine (SHIMADZU, AGS-J, Japan) at a crosshead speed of 0.5 mm min^{-1}. Elastic modulus was calculated as the slope of the initial linear portion of the stress–strain curve.

Samples of CS-SS/HA-s, CS/HA-s and CS-SS/HA-g nanocomposites were made into circular discs suitably sized

(diameter 10 mm, height 1 mm). The MG63 cells (2.0×10^4 cells/well) were seeded on each discs placed in the 24-well plates (Corning Life Sciences). Cells cultivated in the same wells without samples were used as a control. Plates were incubated in Dulbecco's modified Eagle medium (DMEM) containing 10% fetal bovine serum (FBS) at 37 ºC in a 5% CO_2 incubator for 7 days, and the cell viability was studied using cell counting kit-8 assay (CCK-8; Dojindo Laboratories, Japan) according to the manufacturer's instructions. After 1, 3 and 7 days of culture, nanocomposites were gently washed with PBS and then 2 ml of DMEM containing 10% CCK-8 was added per well. The disks were incubated at 37 ºC for 2 h. After incubation, the supernatant was transferred to a 96-well plate and the optical density (O.D.) was measured at 450 nm using an ELX808 Ultra Microplate Reader (Bio-Tek Instruments, Inc., America).

Behaviors of MG63 cells on various CS-SS/HA-s, CS/HA-s and CS-SS/HA-g nanocomposites were studied by SEM. After cultivation for 3 days, composites grown with cells were washed twice with PBS, and cells were fixed with 2.5 wt.% glutaraldehyde under 4 ºC overnight. Fixed samples were dehydrated by ethanol in an increasing concentration gradient (30, 50, 70, 90 and 100 vol.%), followed by lyophilization. The dried samples were glued onto copper stubs, and sputter coated with gold prior to SEM observation.

3 Results and discussion

3.1 Chemical interaction of CS-SS/HA (CS-SS/HA-s and CS-SS/HA-g) nanocomposites and their inorganic phase

Total amino acids in sericin raw material, CS-SS/HA-s and CS-SS/HA-g nanocomposite are provided in Table 2. It is shown that the majority of amino acids in sericin raw material are serine, aspartic acid, threonine and glycine as 25.24%, 14.88%, 7.08% and 6.85%, respectively, which was similar to those in literature report [49-52]. Glutamate and aspartic acid are acidic amino acid present in the sericin. Serine and threonine amino acids that contain hydroxyl side chains together contribute about 41% of the total amino acids present in this sericin. Bulky amino acids such as tyrosine are present in very less amount. Most of the residues present in the protein are either hydrophilic or does not have hydrophobic side groups making the sericin a water-soluble protein. As listed in Table 2, the amino acids in both

CS-SS/HA-s and CS-SS/HA-g nanocomposites mainly consist of serine, aspartic acid, threonine and glycine, which indicated that SS was successfully introduced in the CS-SS/HA-s and CS-SS/HA-g nanocomposites system. Moreover, serine, aspartic acid, threonine and glycine account for 32.36%, 19.08%, 9.08% and 8.78% respectively, of the total amino acids present in this sericin. However, they fall to 27.49%, 18.87%, 7.00% and 8.63% respectively, in CS-SS/HA-s nanocomposite, and descend to 23.08%, 16.57%, 6.21% and 7.10% respectively, in CS-SS/HA-g nanocomposite. Therefore, it could be concluded that the interaction between these amino acids and inorganic hydroxyapatite occurred after composition, which resulted from that these four kinds of amino acids contain hydroxyl and carboxyl side chains that could induce the nucleation and regulated the growth of HA.

Fig. 2a-c shows the FTIR spectra of the CS-SS/HA-s (Fig. 2a), the inorganic phase of the CS-SS/HA-s nanocomposite (Fig. 2b) and CS-SS/HA-g nanocomposite (Fig. 2c). In Fig. 2a-c, the characteristic peaks of HA were captured at around 1096 cm^{-1}, 1037 cm^{-1} and 965 cm^{-1}, which were ascribed to the P–O stretching vibration modes, whereas the bands at 603 cm^{-1} and 567 cm^{-1} to the O–P–O bending mode, both were considered to be from the PO_3^{4-} group in HA crystals. The bands at 3570 cm^{-1} and 632 cm^{-1} represented hydroxyl group as stretching and bending vibration, while the peaks at around 870 cm^{-1}, 1418 cm^{-1} and 1456 cm^{-1} were ascribable to the C–O stretching vibration mode on the CO_3^{2-} group, which agreed with the fact that HA crystals prepared using the precipitation method contained carbonate ions [53].

FTIR is a powerful tool for the study of secondary and tertiary structure and conformational transitions of polypeptides and proteins [54]. As shown in Fig. 3a, the characteristic amide peaks of the SS appear at 1656 cm^{-1} (amide I), 1542 cm^{-1} (amide II) and 1246 cm^{-1} (amide III), which were ascribed to the typical peaks of random coil structure. In SS, the amide I absorption band was primarily derived from the C=O stretching vibration of the amide groups . The amide II absorption band was due to the N–H bending and C–N stretching vibrations, and the amide III aroused from the C–N stretching and C=O bending vibrations. Another two bands at 1398 cm^{-1} and 1075 cm^{-1} were assignable to the C–H and O–H bending vibrations and the C–OH stretching vibration, respectively, both of which were

208 due to the side-chain of abundant serine residues in the sericin [55]. When compared with the amide I (-$CONH_2$) and
209 amide I (C=O) band in the FTIR spectrum of pure CS (Fig. 3b) at 1642 cm^{-1} and 1600 cm^{-1}, the appearance of the
210 characteristic absorption peak in the spectrum of the CS-SS/HA-s nanocomposite (Fig. 3c) at 1634 cm^{-1} (amide I) and
211 1542 cm^{-1} (amide II) was remarkable, indicating that SS was successfully introduced in the CS-SS/HA-s nanocomposite
212 system. Based on the literature report [56] and the above FTIR analysis of SS, it could be concluded that the
213 characteristic absorption bands at 1634 cm^{-1} and 1542 cm^{-1} corresponded to β-sheet conformation and random coil
214 structure respectively. In the CS-SS/HA-s nanocomposite system, SS may participate in the intermolecular crosslinking
215 reaction of CS after the addition of genpin. The formation of the intermolecular crosslinking network structure resulting
216 from the crosslinking reaction between abundant serine residues of SS and CS may limit the intramolecular crosslinking
217 of SS to a certain extent. The structure of SS molecules in the hydrogel may transform into β-sheet when intramolecular
218 cross-linking occurred [49]. However, the β-sheet and random coil structure coexist in CS-SS/HA-s nanocomposite,
219 indicating that SS molecules partially involved in the intermolecular crosslinking while a part of SS molecules were
220 concerned in intramolecular crosslinking as a result of hydrogen bond interaction. Moreover, the peak of amide III
221 almost disappeared in the CS-SS/HA-s (Fig. 3c) and CS-SS/HA-g nanocomposites (Fig. 3d) by comparison between
222 pure SS (Fig. 3a) and composites, which suggested that the carbonyl (C=O) bonds could serve as the initial nucleation
223 site of crystals [57].

224 Inorganic phase composition of CS/HA-s (Fig. 4a), CS-SS/HA-s (Fig. 4b) and CS-SS/HA-g (Fig. 4c) nanocomposite
225 were measured by using XRD (Fig. 4). The predominant crystal phase of all samples was HA corresponding to the
226 Powder Diffraction File (PDF Card No. 9-432). The peaks of crystal phases at 25.9°, 32° and 39.7° (2θ) are assignable
227 to (002), (211) and (310) of crystalline HA, respectively. As shown in Fig. 4a-c, three samples revealed broad peaks
228 with poor crystallinity around the characteristic diffraction region near 32° (2θ), which signified that HA had low
229 crystallinity in all samples. This crystallographic structure of three samples was more similar to natural bone mineral
230 (biological apatite) [58]. The reason for the low crystallinity of precipitated HA in all samples might be the size effect

owing to the three-dimensional network microstructure provided by the crosslinked CS-SS hydrogel, where the growth of inorganic crystal was limited. In spite of this, CS-SS/HA-s nanocomposite possessed higher crystallinity than CS/HA-s nanocomposite based on (211) peak, indicating the possibility of different preferential orientation growth in the presence of SS.

3.2 Morphology of CS-SS/HA (CS-SS/HA-s and CS-SS/HA-g) nanocomposites and their formation mechanism

Fig. 5a-f shows the SEM morphologies of the CS-SS/HA-s, CS/HA-s and CS-SS/HA-g nanocomposites. From the SEM results of the CS-SS/HA-s nanocomposite (Fig. 5a,b), it could be observed that inorganic crystals of HA are tightly bonded with the CS-SS matrix, because no interface between the inorganic and organic phases can be distinguished. It is difficult to get this decentralization effect by conventional mechanical mixing or co-precipitation [56,59]. The inorganic particles exhibited as rod-like crystals whose size was over 200 nm in length and 20–50 nm in diameter. However, the SEM images for the CS/HA-s nanocomposite where many spherical particles were found are presented in Fig. 5c,d. This signifies that SS was responsible for the formation of the uniform rod-like HA nanoparticles. Compared with the CS-SS/HA-s system partially, there were not only rod-like crystals but also several micropores whose diameters ranged from 100 to 400 nm in the CS-SS/HA-g nanocomposites (Fig. 5e.f). In our work, CS hydrogel played an important role in the regulation and decentralization of inorganic nanoparticles through its compartment effect. SS was responsible for the formation of the uniform rod-like HA nanoparticles.

The mechanisms for the formation of the rod-like HA nanoparticles in the CS-SS/HA-s and CS-SS/HA-g nanocomposite were proposed in Fig. 6. In this study, due to the compartmental effect, CS hydrogel acted a significant role in the dispersion of Ca^{2+}, PO_4^{3-} and SS nanoparticles within crosslinked CS hydrogel. Furthermore, many studies have reported that hydroxyapatite deposition can be initiated by functional groups existing on the surface of a material [60, 61]. SS, a globular protein, has more polar side groups such as carboxyl, hydroxyl, and amino groups from a comparison of the amino acid content between silk sericin and silk fibroin, which lend it to heterogeneous nucleation of apatite [62-64]. With the increase of pH after the addition of ammonia solution or NH_3 gas diffusion, a large number of

254 polar side groups on silk sericin, such as carboxyl, hydroxyl, and amino groups, may begin to act as nucleation center
255 for HA formation. These negatively charged residue groups can interact with Ca^{2+} ions. The PO_4^{3-} ions can bond Ca^{2+}
256 ions through strong electrostatic interaction and thus form a local supersaturation microenvironment. The electrostatic
257 interaction between Ca^{2+} and PO_4^{3-} ions was alternate, thus this self-assembly behavior increased the number of
258 inorganic ions to form the rod-like nanoparticles. It is also noteworthy that the rate of NH_3 gas diffusion in the
259 CS-SS/HA-g system was slower than that in the CS-SS/HA-s system, leading to slow mineralization process which may
260 form less rod-like nanoparticles in a time frame. Hence, the growth of apatite could be existed just along scaffold of
261 organic hydrogel itself, so the pores among the rod-like nanoparticles probably appeared within the limited
262 three-dimensional (3D) network microstructure provided by crosslinked CS hydrogel. Moreover, the compartment
263 effect of crosslinking CS hydrogel, which owned 3D network microstructure limited the excessive growth of the
264 rod-like HA particles, so the inorganic nano-particles were limited to aggregate in the compartment of the CS hydrogel
265 template. To sum up, such a double temple based on the hydrogel and the intensive heterogeneous nucleation sites of SS
266 has a distinct influence on the formation of homogeneous rod-like nanocomposites.

267 On the other hand, Ca^{2+} and PO_4^{3-} ions were inclined to bond with carbonyl and amino groups on the compartment
268 walls of the CS hydrogel network in the absence of silk seicin, and it was hard to form a high electrostatic field
269 concentration because of the irregular nucleation sites. Consequently, the nanocomposite participated by the CS
270 hydrogel temple alone couldn't come into being such special rod-like nanocomposites.

271 Especially, the size of CS-SS/HA-g nanocomposite (organic/inorganic=30/70) macropores was bigger than that of
272 CS-SS/HA-g nanocomposite (organic/inorganic=70/30). As SEM photographs illustrated (Fig. 7a,b), with the increase
273 of inorganic component content in the nanocomposites, the size of macropores increased from 100 to nm 500 nm. As
274 inorganic component content in the nanocomposites increased, the pores of organic hydrogel were full of more and
275 bigger rod-like nano particles gradually, the size of the 3D network lattice became smaller, so the size of macropores
276 decreased accordingly. These morphological changes were also in agreement with previous conclusion (Fig. 6).

The morphologies of CS-SS/HA-s nanocomposite and CS-SS/HA-g nanocomposite were also examined using TEM (Fig. 8a,c). The results revealed that the rod-like crystals were formed in all the samples. Furthermore, through the observation of highly magnified TEM image of crystal lattice (Fig. 8b), it indicated that CS-SS/HA-s nanocomposites had more precise bonding at 2-5 nm level, and nano-scale sub-crystallites in organic matrices had no uniform crystallographic orientation. The polycrystal diffraction ring and amorphous spots shown in the inset of TEM selected area electron diffraction pattern also accorded with the structure in Fig. 8b. It can be believed that the strong combination of two phases from nano-sized to submicron level would benefit to ideal stress impress and increase of mechanical strength, while the random crystallographic orientation of the nanoparticles may be responsible for the isotropic character of the composite. In Fig. 8b, the uniform lattice spacing was 0.344 nm, indicating that the rod-like HA crystal of CS-SS/HA-s nanocomposite was (002) direction. Lattice spacing of 0.281 nm at right-bottom indicated that a crystal face of (211) existed. The result was consisted with Fig. 4, in which the strong diffraction peaks of (002) and (211) were observed. As is shown in Fig. 8d, Lattice spacing of 0.281 nm at right-top meant that a crystal face of (211) existed in CS-SS/HA-g nanocomposite, which also accorded with Fig. 4.

3.3 Mechanical properties of CS-SS/HA-s nanocomposites

In dry state, the mechanical properties of the CS-SS/HA-s and CS/HA-s nanocomposites with different organic/inorganic weight ratios were tested by a universal testing machine. Fig. 9a,b shows the elastic modulus and compressive strength data of all the samples with different organic/inorganic weight ratios ranging from 30/70 to 70/30. All the tests were conducted under a compressive load at 0.5 mm/min. The data demonstrated that all the CS-SS/HA-s nanocomposites presented similar mechanical behaviors, with higher elastic modulus and compressive strength than the CS/HA-s nanocomposites at the same organic/inorganic ratio. Nevertheless, when the organic component content was below 50%, both the CS–SS/HA-s and CS/HA-s nanocomposites exhibited low compressive strength, which resulted from the brittleness of hydroxyapatite.

To our knowledge, there are a number of factors affecting the mechanical properties of the organic/inorganic

composites, for instance, particle size, particle shape, particle dispersion, the inherent mechanical behavior of the organic component, the organic/inorganic weight ratio, and the interfacial interactions between the organic and inorganic components. Although silk sericin mechanically fragile in nature [65], the elastic modulus and compressive strength of CS–SS/HA-s nanocomposites were both enhanced compared with CS/HA-s nanocomposites after incorporating with SS, which may attribute to the following factors: (1) the rod-like HA nanoparticles as an inorganic reinforcement phase; (2) SS could control the crystal orientation and provides a bridge between CS and HA; (3) the strong interfacial interaction between inorganic and organic phase gained from the in situ precipitation method.

3.4 Characterization of CS-SS/HA-s nanocomposite scaffold

Hydrogel based scaffolds are gaining more and more attention in the field of tissue engineering in recent years [66-68]. The hydrogel scaffolds have an inherent ability to swell in aqueous medium thus permitting the transportation of enzymes and nutrients to and through the scaffolds [69, 70]. In this work a multilevel freeze-drying technique was adopted to obtain a porous CS-SS/HA-s nanocomposite scaffold. The freeze-drying technique consists of freezing an aqueous suspension followed by sublimation of the solidified phase and has been used widely to obtain porous structures [71-74]. The pore size and shape are controlled by the freezing rate and ice growth direction. The scaffold was prepared by lyophilization as shown in Fig. 10. The hydrogel exhibited an opaque structure consisting of water (Fig. 10a). From the SEM images shown in Fig. 10b-e, the scaffold presented a unique multi-level porous structure in which micro- and macro-pores were co-existed. At the macro-structure level, the freeze-dried hydrogel consisted of unidirectional macro-pores throughout the entire scaffold (Fig. 10b), and the size of macro-pores varied from 50 to 200 μm. At the sub-micro-structure level, several small sub-pores were observed in the SEM image at a high magnification (Fig. 10c-e), the size of which was approximately 1-10 μm. It has been reported that pore diameters of between 15 and 50 μm induce fibrovascular growth, whereas those between 50 and 150 μm stimulate osteoid formation. Significantly, pore diameters in the range of 150-500 μm lead directly to mineralized bone. Thus, pore dimension and interconnectivity are key factors in the structural design of synthetic biomaterials to ensure tissue attachment and

integration [75].

As compared to a scaffold prepared by physically mixing and co-precipitation method, in situ precipitation can obtain close combination between the nanosized inorganic particles and the organic matrices, which improved the mechanical properties to support cell adhesion and physiological loading. In addition, uniformly distributed HA nanoparticles in organic matrices increased the bioactivity and osteoconductivity of the CS-SS/HA-s composite scaffold. At last, the introducing of HA with aosteoconductive, non-toxic and non-inflammatory, which has a unique capability of binding to the natural bone through biochemical bonding, would certainly promote cell proliferation, osteoblastic cell differentiation and the interaction between host bone and grafted material [76]. In conclusion, this unique multi-level porous scaffold with micro- and sub-macro-pores will be a good candidate as a scaffold in bone tissue engineering.

3.5 Cell proliferation and morphology on CS-SS/HA (CS-SS/HA-s and CS-SS/HA-g) nanocomposites

A comprehensive understanding of biocompatibility includes the determination of different parameters like cytotoxicity, mutagenicity, carcinogenicity, hemocompatibility, sensitization, and irritation. Even though cytotoxicity is only one aspect of biocompatibility, cytotoxicity studies are appropriate for screening and evaluation of biocompatibility of new or modified materials to be used for medical devices [77]. In this work, the preliminary biological performance of the CS-SS/HA-s and CS-SS/HA-g nanocomposites was evaluated by *in vitro* culturing of MG63 cells. To evaluate cells proliferation, the cell viability on the different materials was compared. CCK-8 assay values of the MG63 cells on the CS-SS/HA-s nanocomposites and the CS/HA-s nanocomposites (organic/inorganic=40/60) on day 1, 3, and 7 were shown in Fig. 11a. In general, the cells on all the materials proliferated with increasing culture time, indicative of good cytocompatibility. However, at each time interval there existed a significant difference in cell proliferation among the samples. CS-SS/HA-s nanocomposites gave the best proliferation result after culturing for 1, 3 and 7 days, while the CS/HA-s nanocomposites yielded the relative low proliferation. It has been reported that sericin enhances proliferation and attachment of mammalian cell, insect lines and hybridoma cells [30]. It was also found to enhance the attachment of cultured human skin fibroblasts. In 2005,

346 Tsubouchi et al. also reported that living fibroblast cells increased to 250% of the control after 72 h. It was, therefore,
347 considered for a role in the healing process of skin lesions [78].

348 Based on these results, when CS-SS/HA-s and CS/HA-s nanocomposite are equal in the weight ratio of calcium
349 phosphate, CS-SS/HA-s nanocomposite showed better osteoblasts compatibility than CS/HA-s nanocomposite, and is
350 more suitable to be used in bone tissue engineering. The main reason of this might be that SS addition increased the
351 biocompatibility [26, 79]. Moreover, it is of noteworthy that the number of cells on both CS-SS/HA-s and CS/HA-s
352 nanocomposite proliferated with increasing culture time, indicating their good cytoactive, which might be credited to
353 HA's good bioactivity. It has been reported that calcium phosphates play a role in increased proliferation of osteoblasts
354 [80-82]. The cellular responses to a biomaterial, such as attachment, proliferation and differentiation, depend not only
355 on physical status (surface morphology, porous structure, porosity and so on) but also on the chemical composition of
356 the biomaterial [83]. The chemical composition, which was relevant to the cell-material interaction, plays crucial roles
357 in determining the cell responses to the biomaterial [84]. In this study, the proliferation of CS-SS/HA-g nanocomposites
358 with different organic/inorganic weight ratios cultured for 1, 3, and 7 days was compared by CCK-8 assay. The data are
359 shown in Fig. 12a. Similarly, the cells on all the samples proliferated with increasing culture time, indicative of good
360 cytocompatibility. More importantly, the proliferation of cells on CS-SS/HA-g nanocomposites increased markedly
361 with an increase of organic/inorganic weight ratios from 30/70 to 70/30, indicating that the organic compositions could
362 enhance the cell affinity of the CS-SS/HA-g nanocomposites. Similar result has been reported that SS/HA films had
363 higher ability to accelerate MG63 cell proliferation than HA films, and an obvious SS concentration-dependent increase
364 of OD_{570} values existed [56]. In addition, as shown in Fig. 11a and Fig. 12a, the OD_{450} value of CS-SS/HA-s
365 nanocomposite (organic/inorganic=40/60) was little higher than that of CS-SS/HA-g nanocomposite
366 (organic/inorganic=40/60) cultured for the same time, which implied that cell proliferation on the former was better
367 than the latter.

368 SEM observation of cell cultures to evaluate morphologic changes is most frequently used in cytotoxicity evaluation

of biomaterials [85, 86]. Fig. 11b-k reveals that MG63 cells cultured for 3 days adhered on the surface of CS-SS/HA-s and CS/HA-s nanocomposites with different organic/inorganic weight ratios. Clearly, it can be observed that MG63 cells exhibited fusiform or polygonal morphology and distributed well on all the samples. Furthermore, MG63 cells re-established cell-cell contacts and formed aggregates on the CS-SS/HA-s nanocomposites, which meant that CS-SS/HA-s nanocomposite was propitious to the attachment and growth of MG63 cells. SEM images of 3-day-cultured MG63 cells on CS-SS/HA-g nanocomposites are shown in Fig. 12b-f. It is evident that MG63 cells grew and spread well on the surface of all samples. These cells, showing a typical polygonal shape, formed a cellular layer with the filopodia anchored to the CS-SS/HA-g nanocomposites and were in contact with each other. The results of SEM indicated that CS-SS/HA-g nanocomposite has good cytocompatibility. Moreover, Fig. 13a-f shows representative SEM morphologies of MG63 cells grown on the CS-SS/HA-s nanocomposites after 1, 3 and 7 days. MG63 cells adhered to the CS-SS/HA-s disc and spread by pseudopodia after 1 day (Fig. 13a,b). Then, they began to spread with fusiform or polygonal morphology and extended some pseudopods to contact each other after 3 days (Fig. 13c,d). After 7 days, MG63 cells rapidly proliferated and grew in an aggregated, multilayered form (Fig.13 e,f). Meanwhile, it is obvious that the cells number within 7 days was more than the number of cells after one day, which also corresponded with the results of the CCK-8 assay (Fig. 11a). This result implied that the CS-SS/HA-s nanocomposite can promote osteoblast attachment, adhesion and proliferation. Although *in vitro* study in this research were relative preliminary, the above researches have indicated that CS-SS/HA nanocomposite (CS-SS/HA-s and CS-SS/HA-g) was more suitable to be used in bone tissue engineering, and *in vitro* study would establish an experimental base for further *in vivo* animal tests.

4 Conclusions

CS-SS/HA-s and CS-SS/HA-g nanocomposites were obtained via a new in situ precipitation method. The introduction of SS in the CS matrix greatly had a large influence on the nucleation and the growth of HA crystalline.

Such a double temple based on the CS hydrogel and the intensive heterogeneous nucleation sites of SS played an important role in the fabrication of the CS-SS/HA-s and CS-SS/HA-g nanocomposites. The CS-SS/HA-s nanocomposite exhibited a homogeneous structure, with special rod-like nanoscale hierarchical features. In addition, the way of alkali diffusion also affected the morphology of the nanocomposites obviously. There were not only rod-like crystals but also several micropores in the CS-SS/HA-g nanocomposites. With SS addition, the CS-SS/HA-s nanocomposites dispalyed much better mechanical behaviors, as confirmed by measuring their elastic modulus and compressive strength. The osteoblast-like MG63 cells cultured on the two kinds of nanocomposites grew and spread actively. The proliferation of the cells, performed directly on the CS-SS/HA-s nanocomposites, showed a higher value than that of the CS/HA-s and CS-SS/HA-g nanocomposites. The present study may provide more theory basis for further enhance the understanding of biomineralization and promote the development of new biomaterials for bone tissue engineering.

Acknowledgements

This research was supported by the National Natural Science Foundation of China (Nos. 31071265 and 30900297) and the Research Fund for the Doctoral Program of Higher Education (No. 20090141120055).

References

[1] D. W. Cole, T. A. Ginn, G. J. Chen, B. P. Smith, W. W. Curl, D. F. Martin and G. G. Poehling, *Arthroscopy*, 2005, **21**, 786.

[2] P. Giannoudis, H. Dinopoulos and E. Tsiridis, *Injury*, 2005, **36**, 20.

[3] X. Li, L. Wang, Y. B. Fan, Q. L. Feng, F.Z. Cui and F. Watari, *J. Bio. Med. Mater. Res. A*, 2013, **101**, 2424.

[4] M. Peter, N. Ganesh, N. Selvamurugan, S. V. Nair, T. Furuike, H. Tamura and R. Jayakumar, *Carbohydr. Polym.*, 2010, **80**, 687.

[5] R. A. A. *Carbohydr. Polym.*, 2009, **77**, 1.

[6] R. Jayakumar, M. Prabaharan, P. T. S. Kumar, S. V. Nair and H. Tamura, *Biotechnol. Adv.*, 2011, **29**, 322.

[7] M. C. Yang, S. S. Wang, N. K. Chou, N. H. Chi, Y. Y. Huang, Y. L. Chang, M. J. Shieh and T. W. Chung, *Biomaterials*, 2009, **30**, 3757.

[8] Q. Yao, P. Nooeaid, J. A. Roether, Y. Dong, Q. Zhange and A. R. Boccaccini, *Ceram. Int.*, 2013, **39**, 7517.

[9] J. K. F. Suh, H and W. T. Matthew, *Biomaterials*, 2000, **21**, 2589.

[10] I. F. Amaral, M. Lamghari, S. R. Sousa, P. Sampaio and M. A. Barbosa, *J. Biomed. Mater. Res. A*, 2005, **75**, 387.

[11] J.G. Hardy and T.R. Scheibel, *Prog. Polym. Sci.*, 2010, **35**, 1093.

[12] G. Tripathi and B. Basu, *Ceram. Int.*, 2012, **38**, 341.

[13] L. L. Hench, *J. Am. Ceram. Soc.*, 1998, **81**, 1705.

[14] F. Scalera, F. Gervaso, K. P. Sanosh, A. Sannino and A. Licciulli, *Ceram. Int.*, 2013, **39**, 4839.

[15] Q. Wu, X. Zhang, B. Wu and W. Huang, *Ceram. Int.*, 2013, **39**, 2389.

[16] B. Li, L. N. Huang, X. B. Wang, J. H. Ma, F. Xie and L. Xia, *Ceram. Int.*, 2013, **39**, 3423.

[17] W. Tachaboonyakiat, T. Serizawa and M. Akashi, *Polym. J.*, 2001, **33**, 177.

[188] X. B. Zhang, L. X. Zhu, H. Lv, Y. L. Cao, Y. Liu, Y. Xu, W. M. Ye and J. Wang, *J. Mater. Sci. Mater. Med.*, 2012, **23**, 1941.

[19] R. Dash, S. K. Ghosh, D. L. Kaplan and S. C. Kundu, *Comp. Biochem. Physiol. Part B: Biochem. Mol. Biol.*, 2007, **147**, 129.

[20] T. Khire, J. Kundu, S.C. Kundu and V.K. Yadavalli, *Soft. Matter.*, 2010, **6**, 2066.

[21] H. Teramoto, K. Nakajima and C. Takabayashi, *Biosci. Biotechnol. Biochem.*, 2005, **69**, 845.

[22] R. Dash, M. Mandal, S. Ghosh and S. Kundu, *Mol. Cell. Biochem.*, 2008, **311**, 111.

[23] R. Dash, C. Acharya, P. Bindu and S. Kundu, *B. M. B. Rep.*, 2008, **41**, 236.

[24] A. Tekeuchi, C. Ohtsuki, T. Miyazaki, H. Tanaka, M. Yamazaki and M. Tanihara, *J. Biomed. Mater. Res.*, 2003, **65A**, 283.

[25] P. Aramwit, S. Kanokpanont, W. De-Eknamkul, K. Kamei and T. Srichana, *J. Biomater. Sci. Polym. Ed.*, 2009, **20**,

1295.

[26] P. Aramwit, S. Kanokpanont, T. Nakpheng and T. Srichana, *Int. J. Mol. Sci.*, 2010, **11**. 2200.

[27] P. Aramwit, S. Kanokpanont, W. De-Eknamkul and T. Srichana, *J. Biosci. Bioeng.*, 2009, **107**, 556.

[28] S. Terada, M. Sasaki, K. Yanagihara and H. Yamada, *J. Biosci. Bioeng.*, 2005, **100**, 667.

[29] N. Minoura, S. Aiba, Y. Gotoh, M. Tsukada and Y. Imai, *J. Biomed. Mater. Res.*, 1995, **29**, 1215.

[30] S. Terada, T. Nishimura, M. Sasaki, H. Yamada and M. Miki, *Cytotechnology*, 2002, **40**, 3.

[31] F. Zhang, Z. Zhang, X. Zhu, E. Kang and K. Neoh, *Biomaterials*, 2008, **29**, 4751.

[32] A. Motta, B. Barbato, C. Foss, P. Torricelli and C. Migliaresi, *J. Bioact. Compat. Polym.*, 2011, **26**, 130.

[33] Q. Zhang, P. Dong, L. Chen, X. Wang and S. Lu, *J. Biomed. Mater. Res. A*, 2013, **102A**. 76.

[34] S. K. Das, T. Dey and S. C. Kundu, *R. S. C. Adv*., 2014, **4**, 2137.

[35] K. Maikrang and P. Aramwit, *I. F. M. B. E. Proc.*, 2009, **23**, 1356.

[36] Y. Song, Y. Jin, J. Sun, and D. Wei, *Polym. Int*., 2006, **55**, 1350.

[37] H. Teramoto, K. Nakajima and C. Takabayashi, *Biomacremolecules*, 2004, **5**, 1392.

[38] X. H. Wang, W. Y. Deng, Y. Y. Xie and C.Y. Wang, *Chem. Eng. J.*, 2013, **228**, 232.

[39] J. Fangkangwanwong, R. Yoksan and S. Chirachanchai, *Polymer*, 2006, **47**, 6438.

[40] G. Tronci, H. Ajiro, S. J. Russell, D. J. Wood and M. Akashi, *Acta Biomater.,* 2014, **10**, 821.

[41] R. F. Liu, X. L. Xu, X. P. Zhuang and B. W. Cheng, *Carbohydr. Polym.*, 2014, **101**, 1116.

[42] J. Y. Lai, Y. T. Li and T. P. Wang, *Int. J. Mol. Sci.*, 2010, **11**, 5256.

[43] J. Y. Lai, *Int. J. Mol. Sci.*, 2012, **13**, 10970.

[44] Y. L. Chang, T. C. Liu and M. L. Tsai, *Int. J. Mol. Sci.*, 2014, **15**, 9979.

[45] S. D. Tommaso, P. David, K. Picolet, M. Gabant, H. David, J. L. Morançais, J.Gomar, F. Leroy and C. Adamo, *RSC Adv.*, 2013, **3**, 13764.

[46] X. Cai, H. Tong, X. Y. Shen, W. X. Chen, J. Yan and J. M. Hu, *Acta Biomater.*, 2009, **5**, 2693.

[47] X. Y. Shen, H. Tong, Z. H. Zhu, P. Wan and J. M. Hu, *Mater. Lett.*, 2007, **61**, 629.

[48] X. Y. Shen, H. Tong, T. Jiang, Z. H. Zhu, P. Wan and J.M. Hu, *Compos. Sci. Technol.*, 2007, **67**, 2238.

[49] M. N. Padamwar and A. P. Pawar, *Pak. J. Sci. Ind. Res.*, 2004, **63**, 323.

[50] K. Tsubouchi, Y. Igarashi, Y. Takasu and H. Yamada, *Biosci Biotechnol Biochem*, 2005, **69**, 403.

[51] Y. Q. Zhang, *Biotechnol. Adv.*, 2002, **20**, 91.

[52] S. Zhaorigetu, M. Sasaki, H. Watanabe and N. Kato, *Biosci. Biotechnol. Biochem.*, 2001, **65**, 2181.

[53] I. R. Gibson and W. Bonfield, *J. Biomed. Mater. Res.*, 2002, **59**, 697.

[54] F. S. Parker, *Application of Infrared Spectroscopy in Biochemistry, Biology and Medicine.* Plenum Press, 1971.

[55] G. He, T. Dahl, A. Veis and A. George, *Nat. Mater.*, 2003, **2**, 552.

[56] Y. R. Cai, J. Jin, D. P. Mei, N. X. Xia and J. M. Yao, *J. Mater. Chem.*, 2009, **19**, 5751.

[57] J. L. Wang, W. Zhou, W. Hu, L. Zhou, S. Q. Wang and S. M. Zhang, *J. Biomed. Mater. Res. Part A*, 2011, **99A**, 327.

[58] J. C. Elliot, in *Studies in inorganic chemistry*, ed. J. C. Elliot, Elsevier Science, Amsterdam, 1994, pp.111.

[59] Y. R. Cai, D. P. Mei, T. Jiang and J. M. Yao, *Mater. Lett.*, 2010, **64**, 2676.

[60] P. Li, C. Ohtsuki, T. Kokubo, K. Nakanishi, N. Soga and K. de Groot, *J. Biomed. Mater. Res.*, 1994, **28**, 7.

[61] T. Kokubo, H. M. Kim, M. Kawashita, H. Takadama, T. Miyazaki, M. Uchida and T. Nakamura, *Glastech. Ber. Sci. Technol.*, 2000, **73C1**, 247.

[62] A. Takeuchi, C. Ohtsuki, T. Miyazaki, M. Kamitakahara, S. Ogata, M. Yamazaki, Y. Furutani, H. Kinoshita and M. Tanihara, *J. R. Soc. Interface.*, 2005, **2**, 373.

[63] K. Shimura and Y. Katagata, in *Structure of silk yarn, part B: chemical structure and processing of silk yarn*, ed. N. Hojo, Science, USA, 2000, pp. 3-20.

[64] K. Komatsu, in *Structure of silk yarn, part B: chemical structure and processing of silk yarn*, ed. N. Hojo, Science, USA, 2000, pp. 21-46.

484 [65] P. Aramwit, T. Siritientong, S. Kanokpanont and T. Srichana, *Int. J. Biolog. Macromol.*, 2010, **47**, 668.

485 [66] L. Gao, H. Gan, Z. Y. Meng, R. L. Gu, Z. N. Wu, L. Zhang, X. X. Zhu, W. Z. Sun, J. Li, Y. Zheng and G. F. Dou,

486 *Colloid. Surface B*, 2014, **117**, 398.

487 [67] Z. Xia, M. M. Villa and M. Wei, *J. Mater. Chem. B*, 2014, **2**, 1998.

488 [68] W. C. Hsieh and J. J. Liau, *Carbohydr. Polym*., 2013, **98**,574.

489 [69] K. Gkioni, S. C. G. Leeuwenburgh, T. E. L. Douglas, A. G. Mikos and J. A. Jansen, *Tissue Eng. Part B*, 2010, **16**,

490 577.

491 [70] H. Tamura, T. Furuike, S. V. Nair and R. Jayakumar, *Carbohydr. Polym.*, 2011, **84**, 821.

492 [71] M. G. Haugh, C. M. Murphy and F. J. O'Brien, *Tissue Eng. Part C*, 2010, **16**, 887.

493 [72] S. Deville, *Adv. Eng. Mater.*, 2008, **10**, 155.

494 [73] D. C. Tuncaboylu and O.Okay, *Langmuir*, 2010, **26**, 7574.

495 [74] H. Zhang and A. I. Cooper, *Adv. Mater.*, 2007, **19**, 1529.

496 [75] D. Green, D. Walsh, S. Mann and R. O. C. Oreffo, *Bone*, 2002, **30**, 810.

497 [76] A. Oladn, F. F. Azhar, *Ceram. Int.*, 2014, **40**, 10061.

498 [77] V. Metzler, H. Bienert, T. Lehmann, K. Mottaghy and K. Spitzer, *A. S. A. I. O. J.*, 1999, **45**, 264.

499 [78] K. Tsubouchi, Y. Igarashi, Y. Takasu and H. Yamada, *Biosci. Biotechnol. Biochem.*, 2005, **69**, 403.

500 [79] S. Dinescu, B. Galateanu, M. Albu, A. Cimpean, A. Dinischiotu and M. Costache, *Int. J. Mol. Sci.*, 2013, **14**, 1870.

501 [80] M. H. Hong, S. M. Kim, J. Y. Om, N. Kwon, Y. K. Lee, *Ann. Biomed. Eng.*, 2014, **42**, 1424.

502 [81] K. Chatterjee, L. Sun, L.C. Chow, M. F. Young, C. G. Simon, *Biomaterials*, 2011, **32**, 1361.

503 [82] P. G. Mitchell, J. A. Struve, G. M. McCarthy, H. S. Cheung, *Arthritis. Rheum.*, 1992, **35**, 343.

504 [83] S. Y. Chou, C. M. Cheng and P. R. Leduc, *Biomaterials*, 2009, **30**, 3136.

505 [84] C. Wu, Y. Ramaswamy, Y. F. Zhu, R. Zheng, R. Appleyard, A. Howard and H. Zreiqat, *Biomaterials*, 2009, **30**,

506 2199.

[85] H. P. Tan, C. R. Chu, K. A. Payne and K. G. Marra, *Biomaterials*, 2009, **30**, 2499.

[86] A. M. Martins, M. I. Santos, H. S. Azevedo, P. B. Malafaya and R. L. Reis, *Acta Biomater.*, 200, **4**, 1637.

Figure Captions

Fig. 1 The synthetic procedures for the fabrication of CS-SS/HA-s and CS-SS/HA-g nanocomposites

Fig. 2 FTIR spectra of (a) the CS-SS/HA-s nanocomposite (organic/inorganic=40/60); (b) the inorganic phase of the CS-SS/HA-s nanocomposite (organic/inorganic=40/60); and (c) the CS-SS/HA-g nanocomposite (organic/inorganic=40/60)

Fig. 3 FTIR spectra of (a) pure SS; (b) pure CS; (c) the CS-SS/HA-s nanocomposite (organic/inorganic=40/60); and (d) the CS-SS/HA-g nanocomposite (organic/inorganic=40/60)

Fig. 4 XRD pattern of (a) the CS/HA-s nanocomposite (organic/inorganic=40/60); (b) the CS-SS/HA-s nanocomposite (organic/inorganic=40/60); and (c) the CS-SS/HA-g nanocomposite (organic/inorganic=40/60)

Fig. 5 SEM micrograghs of (a,b) the CS-SS/HA-s nanocomposite (organic/inorganic=40/60); (c,d) the CS/HA-s nanocomposite (organic/inorganic=40/60); and (e,f) the CS-SS/HA-g nanocomposite (organic/inorganic=40/60)

Fig. 6 Scheme of the formation mechanism of CS-SS/HA-s and CS-SS/HA-g nanocomposites

Fig. 7 SEM micrograghs of the CS-SS/HA-g nanocomposites with different organic/inorganic weight ratios: (a) 30/70; (b) 70/30

Fig. 8 TEM micrograghs of (a,b) the CS-SS/HA-s nanocomposite (organic/inorganic=40/60); the inset shows polycrystall diffraction ring; (c,d) the CS-SS/HA-g nanocomposite (organic/inorganic=40/60)

Fig. 9 Mechanical properties bar graphs of CS/HA-s and CS-SS/HA-s nanocomposites: (a) elastic modulus-organic/inorganic weight ratio bar graph; (b) compressive strength- organic/inorganic weight ratio bar graph (n=3)

Fig. 10 (a) digital photograph of the CS-SS/HA-s hydrogel; and SEM micrograghs of freeze-drying CS-SS/HA-s nanocomposite (organic/inorganic=40/60): (b) primary pores; (c-e) sub-pores

Fig. 11 (a) CCK-8 assay of the proliferation of MG63 cells cultured on the CS/HA-s and the CS-SS/HA-s nanocomposite (organic/inorganic=40/60, n=3); SEM micrographs of MG63 cell morphology on CS/HA-s

553 nanocomposites with different organic/inorganic weight ratios after incubation for 3 days: (b) 30/70; (d) 40/60; (f) 50/50;
554 (h) 60/40; (j) 70/30; and SEM micrographs of MG63 cell morphology on CS-SS/HA-s nanocomposites with different
555 organic/inorganic weight ratios after incubation for 3 days: (c) 30/70; (e) 40/60; (g) 50/50; (i) 60/40; (k) 70/30
556 Fig. 12 (a) CCK-8 assay of the proliferation of MG63 cells cultured on the CS-SS/HA-g nanocomposite with different
557 organic/inorganic weight ratios (n=3); and SEM micrographs of MG63 cell morphology on CS-SS/HA-g
558 nanocomposites with different organic/inorganic weight ratios after incubation for 3 days: (b) 30/70; (c) 40/60; (d)
559 50/50; (e) 60/40; (f) 70/30
560 Fig. 13 SEM micrographs of MG63 cell morphology on CS-SS/HA-s nanocomposites after incubation for different time:
561 (a,b) 1 day; (c,d) 3 days; (e,f) 7 days
562
563
564
565
566
567
568
569
570
571
572
573
574
575

576 **Table Captions**

577 Table 1 The dosage of the reagents

578 Table 2 Amino acid composition of silk sericin, CS-SS/HA-s nanocomposites (organic/inorganic=40/60) and the

579 CS-SS/HA-g nanocomposites (organic/inorganic=40/60)

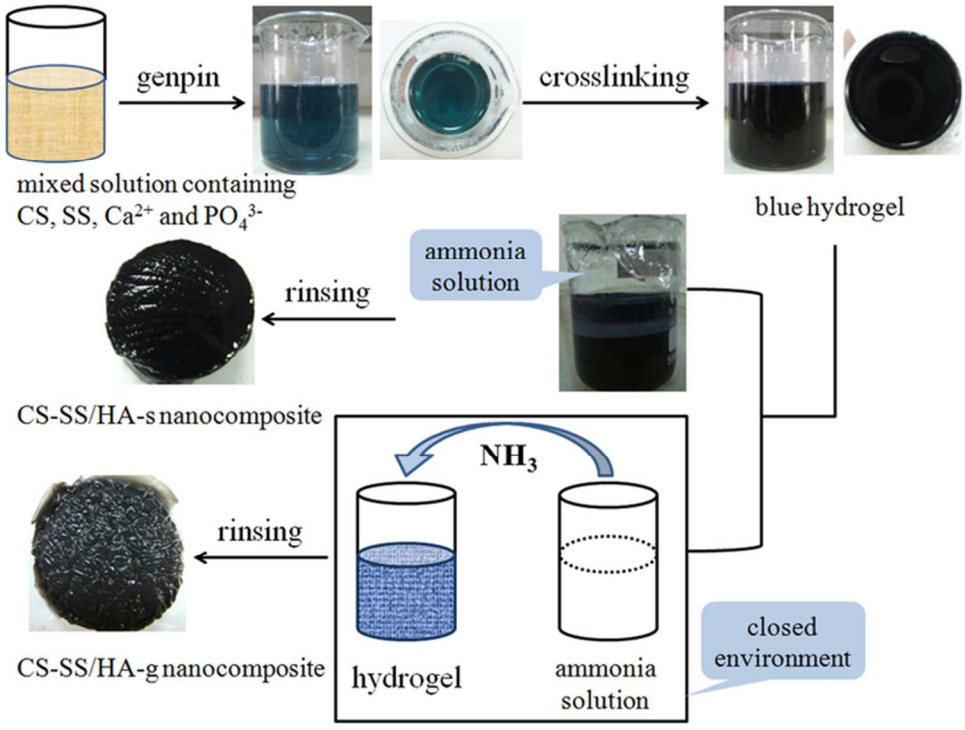

Fig. 1 The synthetic procedures for the fabrication of CS-SS/HA-s and CS-SS/HA-g nanocomposite
67x52mm (300 x 300 DPI)

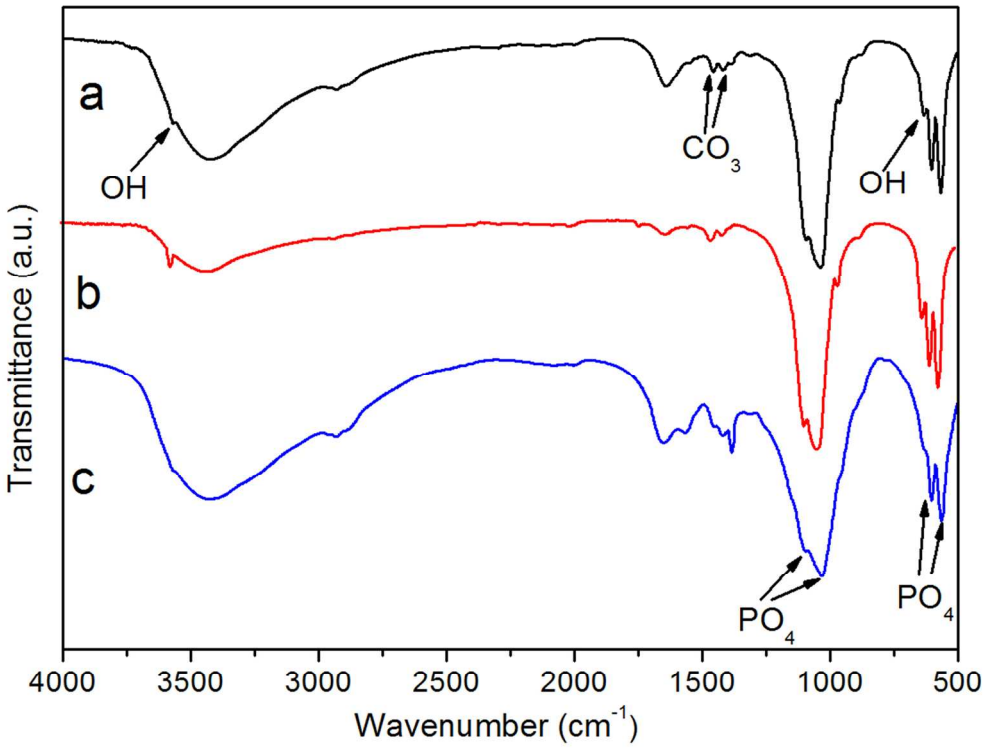

Fig. 2 FTIR spectra of (a) the CS-SS/HA-s nanocomposite (organic/inorganic=40/60); (b) the inorganic phase of the CS-SS/HA-s nanocomposite (organic/inorganic=40/60); and (c) the CS-SS/HA-g nanocomposite (organic/inorganic=40/60)
75x60mm (600 x 600 DPI)

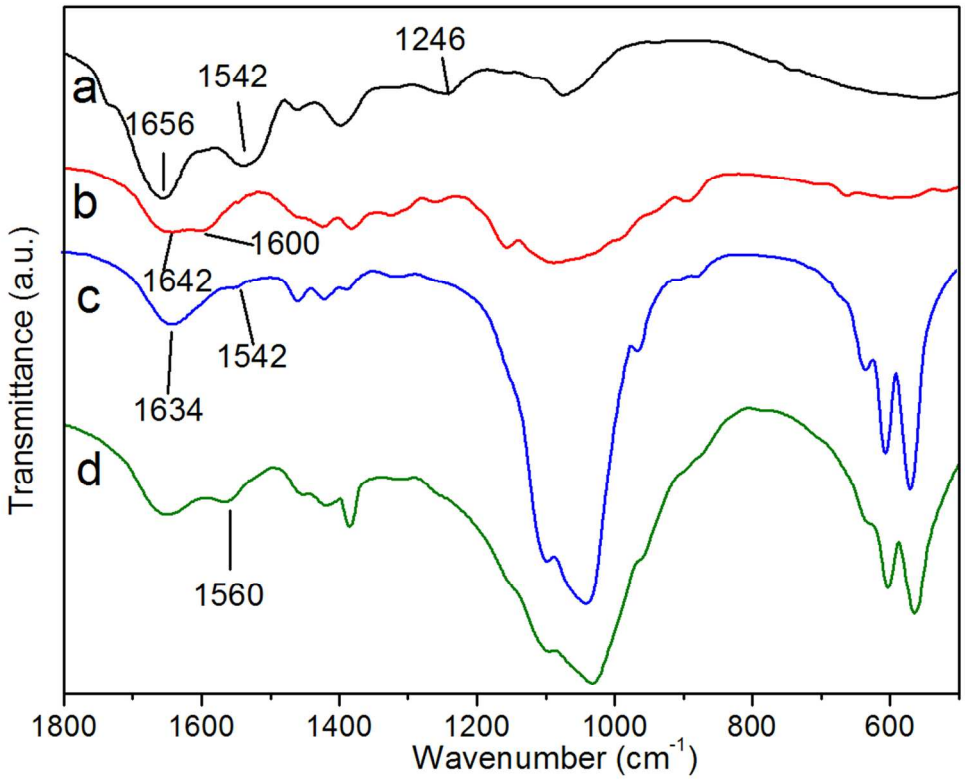

Fig. 3 FTIR spectra of (a) pure SS; (b) pure CS; (c) the CS-SS/HA-s nanocomposite (organic/inorganic=40/60); and (d) the CS-SS/HA-g nanocomposite (organic/inorganic=40/60)
77x62mm (600 x 600 DPI)

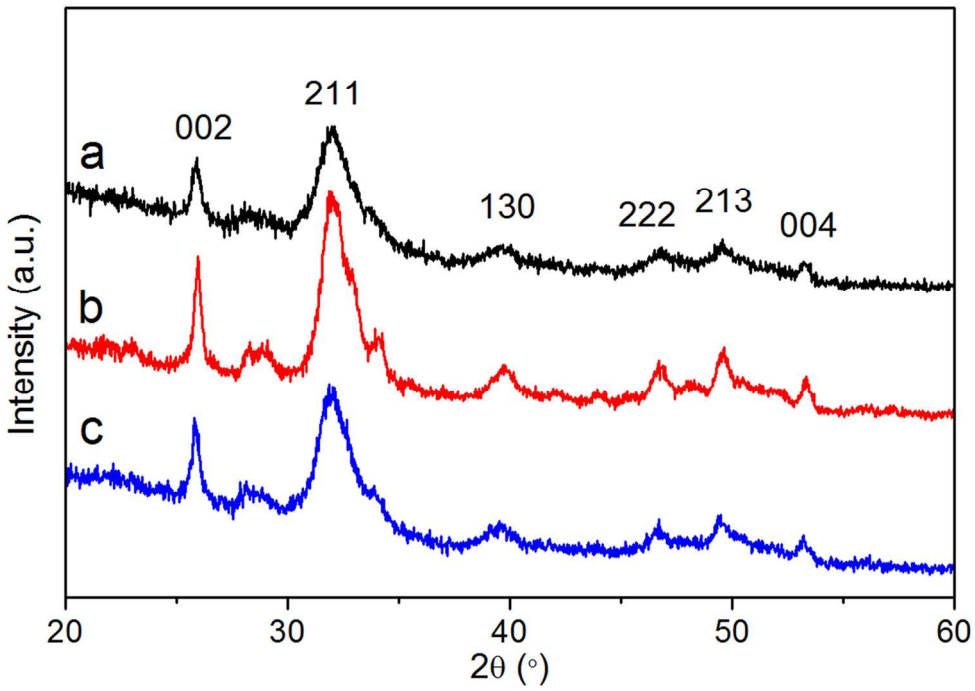

Fig. 4 XRD pattern of (a) the CS/HA-s nanocomposite (organic/inorganic=40/60); (b) the CS-SS/HA-s nanocomposite (organic/inorganic=40/60); and (c) the CS-SS/HA-g nanocomposite (organic/inorganic=40/60)
67x47mm (600 x 600 DPI)

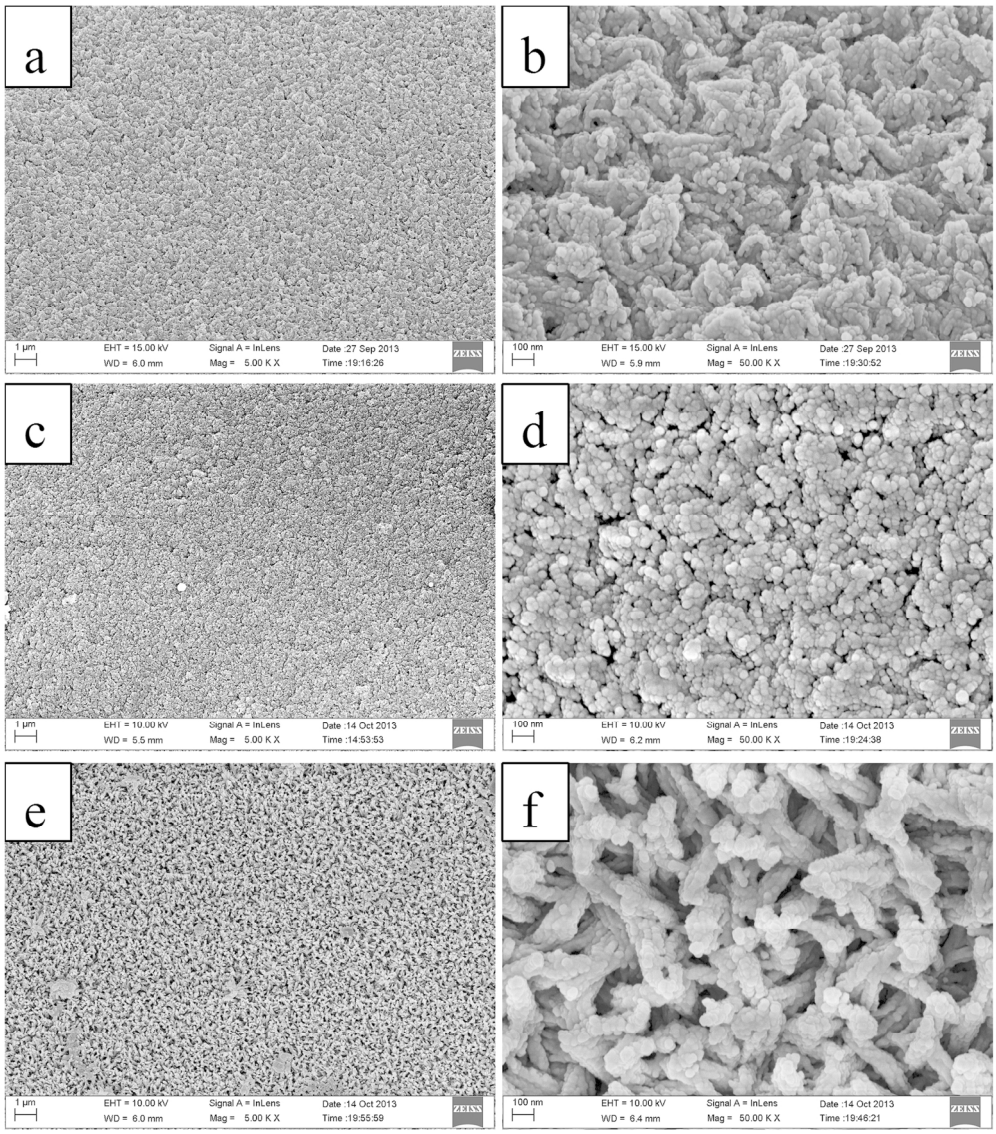

Fig. 5 SEM micrograghs of (a,b) the CS-SS/HA-s nanocomposite (organic/inorganic=40/60); (c,d) the CS/HA-s nanocomposite (organic/inorganic=40/60); and (e,f) the CS-SS/HA-g nanocomposite (organic/inorganic=40/60)
170x194mm (300 x 300 DPI)

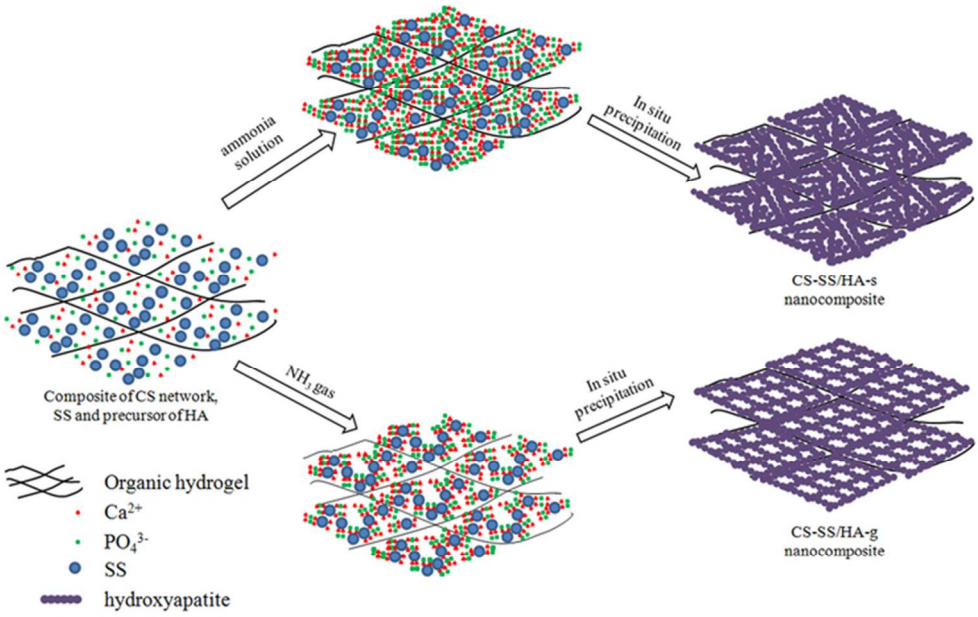

Fig. 6 Scheme of the formation mechanism of CS-SS/HA-s and CS-SS/HA-g nanocomposites
64x41mm (300 x 300 DPI)

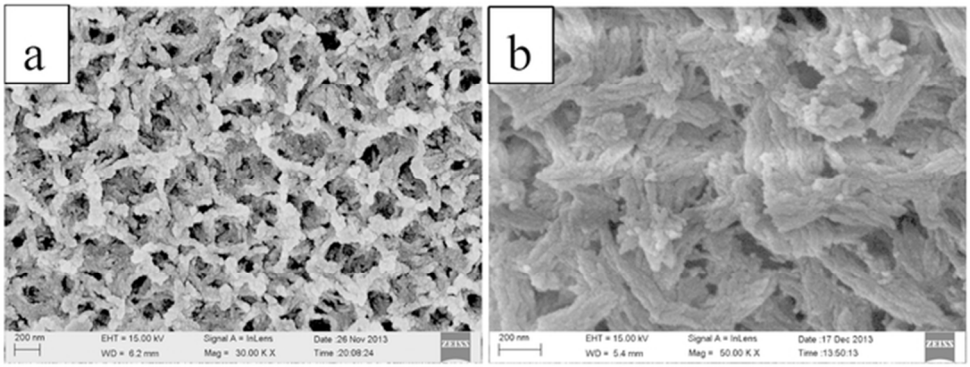

Fig. 7 SEM micrograghs of the CS-SS/HA-g nanocomposites with different organic/inorganic weight ratios: (a) 30/70; (b) 70/30
58x22mm (300 x 300 DPI)

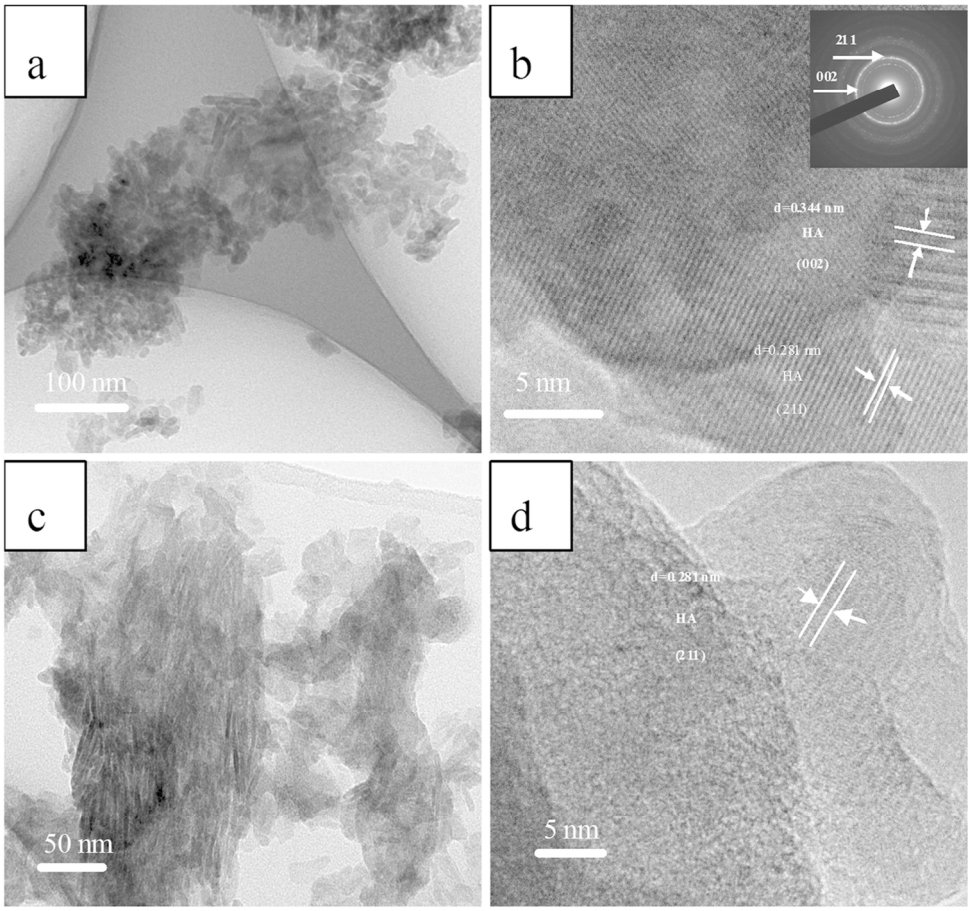

Fig. 8 TEM micrograghs of (a,b) the CS-SS/HA-s nanocomposite (organic/inorganic=40/60); the inset shows polycrystall diffraction ring; (c,d) the CS-SS/HA-g nanocomposite (organic/inorganic=40/60)
117x109mm (300 x 300 DPI)

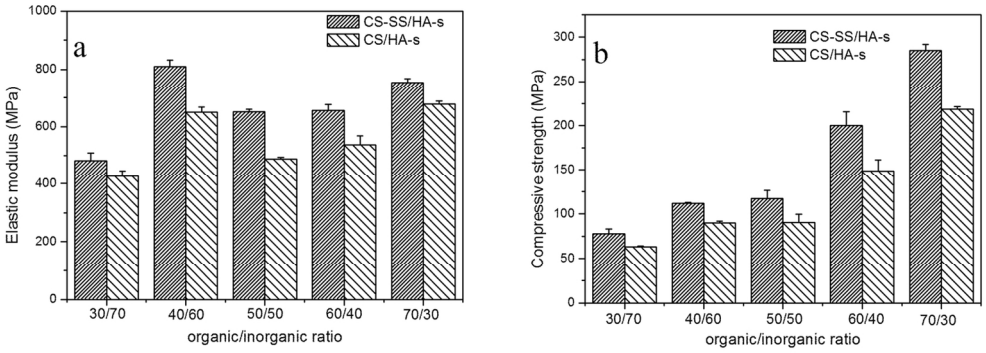

Fig. 9 Mechanical properties bar graphs of CS/HA-s and CS-SS/HA-s nanocomposites: (a) elastic modulus-organic/inorganic weight ratio bar graph; (b) compressive strength- organic/inorganic weight ratio bar graph (n=3)
69x24mm (600 x 600 DPI)

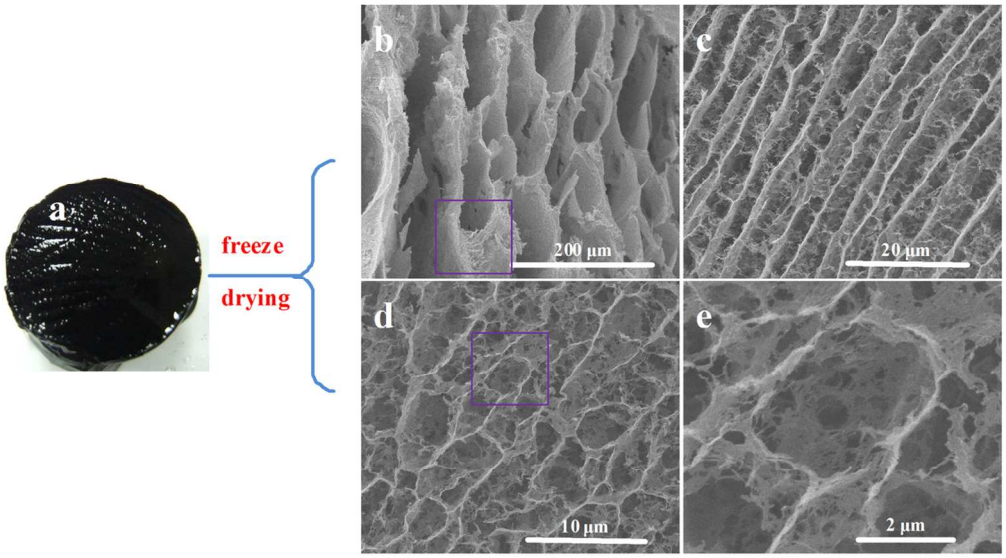

Fig. 10 (a) digital photograph of the CS-SS/HA-s hydrogel; and SEM micrograghs of freeze-drying CS-SS/HA-s nanocomposite (organic/inorganic=40/60): (b) primary pores; (c-e) sub-pores
116x66mm (300 x 300 DPI)

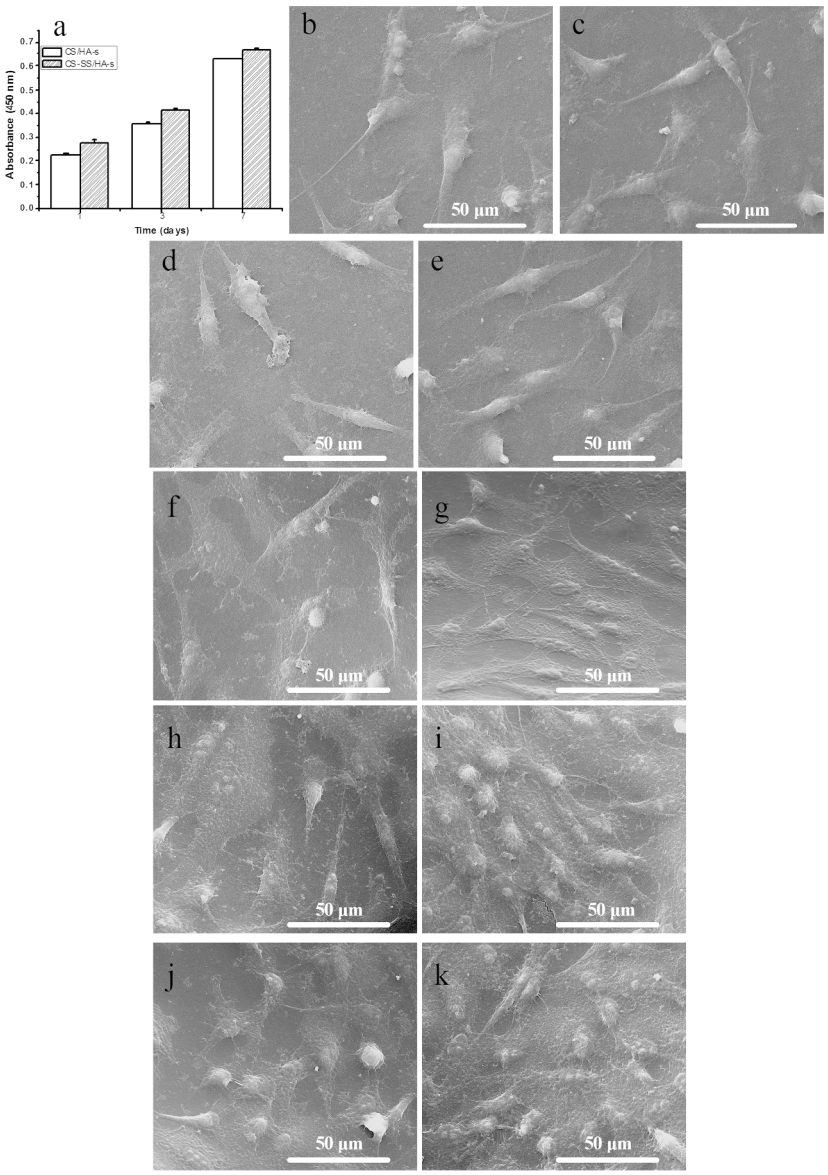

Fig. 11 (a) CCK-8 assay of the proliferation of MG63 cells cultured on the CS/HA-s and the CS-SS/HA-s nanocomposite (organic/inorganic=40/60, n=3); SEM micrographs of MG63 cell morphology on CS/HA-s nanocomposites with different organic/inorganic weight ratios after incubation for 3 days: (b) 30/70; (d) 40/60; (f) 50/50; (h) 60/40; (j) 70/30; and SEM micrographs of MG63 cell morphology on CS-SS/HA-s nanocomposites with different organic/inorganic weight ratios after incubation for 3 days: (c) 30/70; (e) 40/60; (g) 50/50; (i) 60/40; (k) 70/30
245x348mm (300 x 300 DPI)

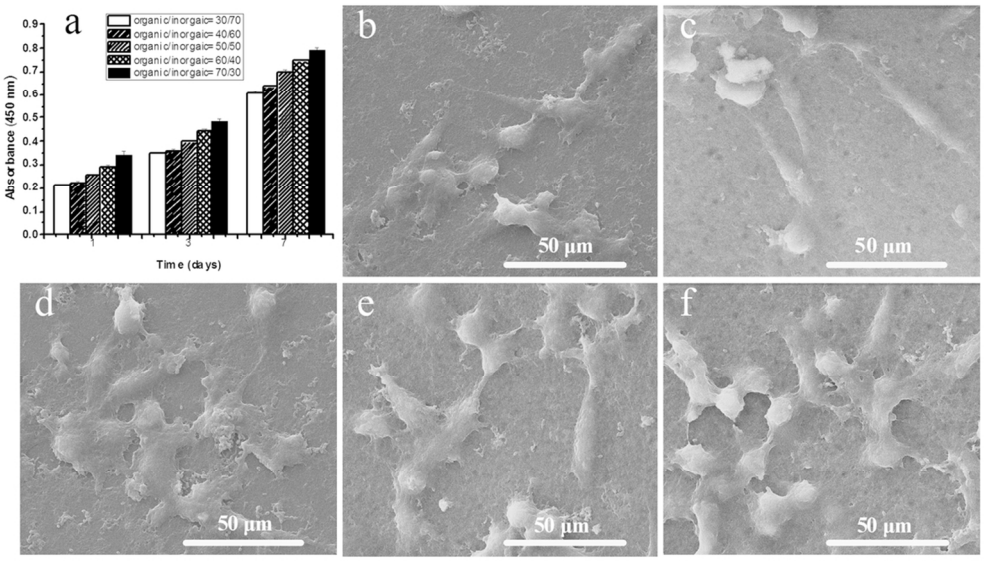

Fig. 12 (a) CCK-8 assay of the proliferation of MG63 cells cultured on the CS-SS/HA-g nanocomposite with different organic/inorganic weight ratios (n=3); and SEM micrographs of MG63 cell morphology on CS-SS/HA-g nanocomposites with different organic/inorganic weight ratios after incubation for 3 days: (b) 30/70; (c) 40/60; (d) 50/50; (e) 60/40; (f) 70/30
100x57mm (300 x 300 DPI)

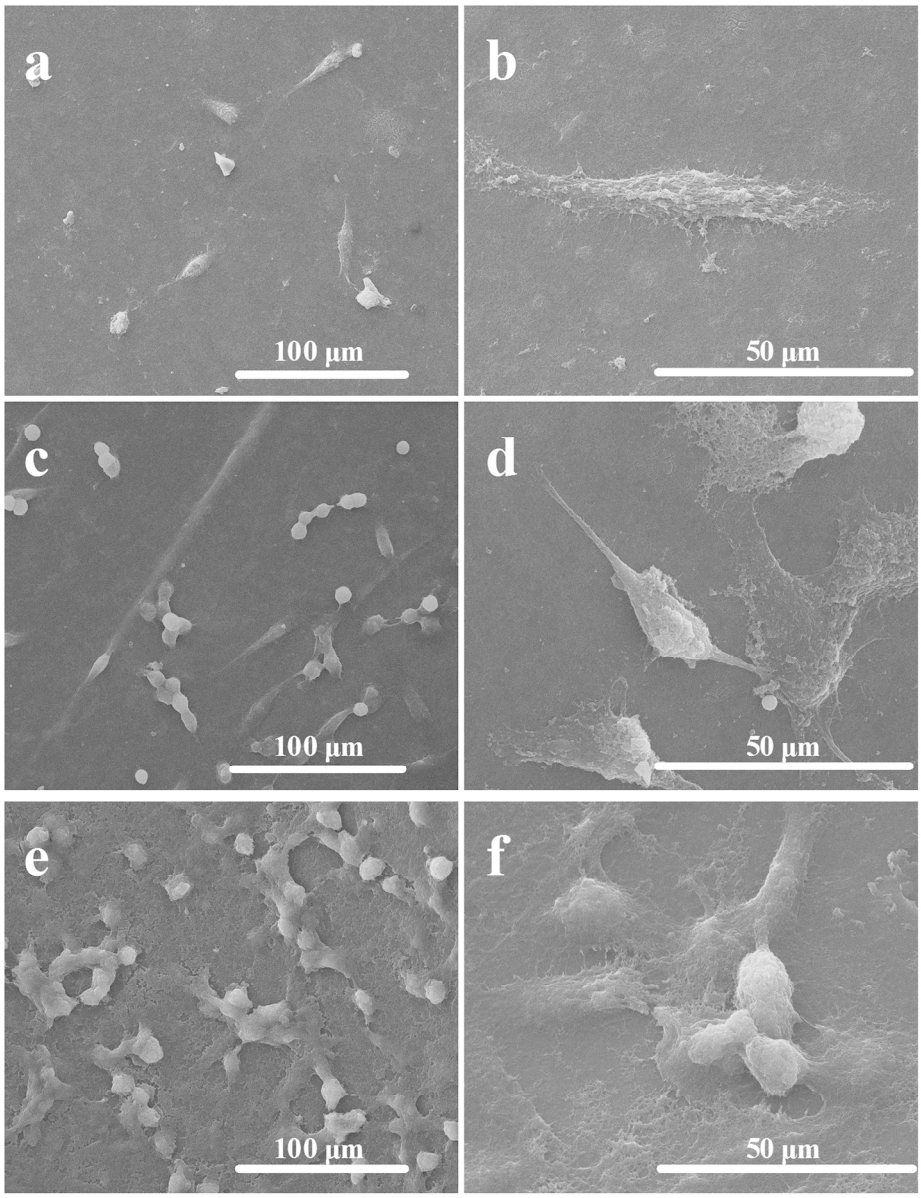

Fig. 13 SEM micrographs of MG63 cell morphology on CS-SS/HA-s nanocomposites after incubation for different time: (a,b) 1 day; (c,d) 3 days; (e,f) 7 days
157x197mm (300 x 300 DPI)

Samples	Organic/HA (weight ratio)	CS (g)	SS (g)	$Ca(NO_3)_2 \cdot 4H_2O$	$(NH_4)_2HPO_4$
CS-SS/HA-s #1 CS-SS/HA-g #2	70/30	0.28	0.28	0.564	0.189
CS-SS/HA-s #3 CS-SS/HA-g #4	60/40	0.24	0.24	0.752	0.252
CS-SS/HA-s #5 CS-SS/HA-g #6	50/50	0.20	0.20	0.940	0.315
CS-SS/HA-s #7 CS-SS/HA-g #8	40/60	0.16	0.16	1.128	0.378
CS-SS/HA-s #9 CS-SS/HA-g #10	30/70	0.12	0.12	1.316	0.441
CS/HA-s #11	70/30	0.56	0	0.564	0.189
CS/HA-s #12	60/40	0.48	0	0.752	0.252
CS/HA-s #13	50/50	0.40	0	0.940	0.315
CS/HA-s #14	40/60	0.32	0	1.128	0.378
CS/HA-s #15	30/70	0.24	0	1.316	0.441

Table 1 The dosage of the reagents
98x62mm (300 x 300 DPI)

Amino acid	Percent of gram amino acid in 100 g protein		
	Sericin raw material	CS-SS/HA-s nanocomposite	CS-SS/HA-g nanocomposite
Aspartic acid	14.88	0.70	0.56
Threonine	7.08	0.26	0.21
Serine	25.24	1.02	0.78
Glutamic acid	5.46	0.33	0.25
Glycine	6.85	0.32	0.24
Alanine	2.94	0.11	0.09
Cystine	0.32	0.24	0.37
Valine	2.77	0.10	0.15
Methionine	0.08	Not detected	Not detected
Isoleucine	0.88	Not detected	Not detected
Leucine	1.08	0.09	Not detected
Tyrosine	2.42	0.14	0.14
Phenylalanine	0.40	Not detected	0.23
Lysine	2.98	0.22	0.20
Proline	Not detected	0.08	0.08
Histidine	1.32	0.04	0.04
Arginine	3.3	0.06	0.04

Table 2 Amino acid composition of silk sericin, CS-SS/HA-s nanocomposites (organic/inorganic=40/60) and the CS-SS/HA-g nanocomposites (organic/inorganic=40/60)
213x291mm (300 x 300 DPI)